ELSEVIER

Comparison between Eulerian and Lagrangian methods to predict brownout clouds

Federico Rovere, George N. Barakos *, René Steijl

CFD laboratory, University of Glasgow, United Kingdom

ARTICLE INFO

ABSTRACT

In this work, brownout simulations using both Lagrangian and Eulerian frames of reference are presented. The work compares results between these two methods and with experimental results. The numerical models used for the carrier and dispersed phases are presented along with the obtained results. Then, follows a description of the simulations performed for brownout clouds around aircraft at different flight configurations. Different flight configurations involve several thrust coefficients, taxiing speeds and the presence of the fuselage. Finally, analyses have been conducted on the influence on the computational efficiency of Eulerian and Lagrangian approaches, and the two models are compared in terms of parallel efficiency. Results show that Eulerian model can be more affordable in terms of computational cost.

1. Introduction

For rotorcraft operating in the desert, the brownout phenomenon is a major risk. Brownout stems from the influence of the rotor wake on loose sediment. When the rotor wake interacts with the ground, dust particles may be uplifted, generating a dense cloud all around the aircraft. The main effect of this cloud, moving around the aircraft, is on the pilot's visual environment. However, the rotorcraft structure and system can also be affected. The lack of pilot visibility defines brownout and whiteout (cloud due to snow) as Degraded Visual Environment (DVE) conditions. In recent years, efforts have been made to help pilots in these situations, developing sensors and advanced cockpit displays. Dynamic roll over and collisions with objects are common accidents due to the low visibility [1,2]. Furthermore, the most common cause of human factor mishaps during military operations is related to brownout [3]. Due to the complexity of these phenomena and the safety issues they may lead to, rotor wakes IGE have been studied using different approaches, both numerical and experimental. Numerical works focus on the possibility to predict the cloud generated by different aircraft configurations (single rotor, tandem or tilt rotor) or flight conditions (different advance ratios and weights) [4–6]. Others tried to define how different manoeuvres may impact on brownout severity [7] [4].

Brownout works may also be divided based on the approach used to predict the dust cloud. The most common approach is Lagrangian, and in this case, every single dust particle is tracked in the flowfield during a simulation. This approach has the advantage to be accurate, especially when particles interact with the ground, ejecting more particles, or when they interact with other rotors or nearby structures. In [8], Tan et al. presented brownout simulations using a Lagrangian model for the particle motion and the vorticity method to solve the flowfield. The approach involves a direct computation of particle-surface and particle-particle interaction, results have been validated with [9] experimental results. Li et al. [10] investigated the possibility to use rotor disk model to simulate brownout clouds [10]. Furthermore, the same research group, in [11], investigated the effect of cross wind on brownout cloud. Lagrangian models have also been used to investigate the effect of different rotor tip shapes on brownout cloud for full-scale hovering rotors [12]. Furthermore, Hu et al. [13] investigated the influence of forces acting on particles including the Saffman and Magnus forces. However, Lagrangian approach may be very expensive due to the huge amount of particles contained in a fully developed brownout cloud. On the other hand, the Eulerian approach considers the dispersed phase as a continuum, usually described using a scalar transport equation, solved after the flowfield model. This approach has also been used in this work. A summary of the literature for the Eulerian-based models used for brownout is presented later in this work. In general, this approach is more affordable in terms of computational cost, but may not be possible to track the particles with enough accuracy to evaluate their interactions with surrounding objects and the ground. However, it may be still possible to evaluate the pilot visual environment and

* Corresponding author.
E-mail addresses: 2420587R@student.gla.ac.uk (F. Rovere), george.barakos@glasgow.ac.uk (G.N. Barakos), rene.steijl@glasgow.ac.uk (R. Steijl).

Nomenclature

Latin

$\boldsymbol{u}$	Flowfield velocity vector, ...	m/s
$\boldsymbol{u}_p$	Particle velocity vector, ...	m/s
A	Bangold model constant, A=0.0123	
a_p	Particle acceleration, ...	m/s^2
B	Ballistic coefficient, ...	kg/m^2
c	Blade chord, ...	m
C_D	Drag coefficient	
C_T	Thrust coefficient, $C_T = \frac{T}{\frac{1}{2}\rho_\infty V_{tip}^2 A}$	
D	Rotor diameter, ...	m
d_p	Particle diameter, ...	μm
$d_\star$	Dimensionless particle diameter	
d_i	Distance between particle and the i-th cell centre, .	m
DL	Disk loading, ...	N/m^2
E	Ratio of erodible to total surface	
F	Vertical flux, ...	$kg/(ms)$
f	Clay fraction	
f_{bi}	Body force in the i-th direction, ...	$kg m/s^2$
g	Gravitional acceleration, $g = 9.81 m/s^2$	
m_p	Particle mass, ...	kg
N_b	Number of blades	
N_p	Number of particles	
Q	Horizontal flux, ...	$kg/(ms)$
R	Rotor radius, ...	m
r_{max}	Maximum distance travelled by the particle during Δt, ...	m
Re	Reynolds number, $Re = V_{tip} c / \nu_\infty$	
$\boldsymbol{S_d}$	Source term, ...	$(N_p)/m^3$
S_p	Frontal particle area, ...	m^2
S_{rotor}	Rotor disk area, ...	m^2
Sc	Schmidt number, $Sc = \nu/D$	
T	Rotor thrust, ...	N
t_f	Fluid characteristic time, ...	s
t_p	Particle characteristic time, ...	s
u^*	Friction velocity, ...	m/s

u_i	Flowfield velocity i-th component, ...	m/s
u_{ri}	Relative particle-fluid velocity i-th component, ...	m/s
w_t	Particle terminal velocity, ...	m/s
u_t^*	Wall friction velocity threshold, ...	m/s
u_{pi}	Particle velocity i-th component, ...	m/s

Greek

β	Bangold model constant, $\beta = 0.0003 \ kg/s^2$	
μ	Advance ratio, $\frac{V_\infty}{V_{tip}}$	
μ^*	Normalized advance ratio, $\frac{\mu}{\sqrt{C_T}/2}$	
ν	Kinematic viscosity, ...	m^2/s
ν_p	Diffusion coefficient, ...	m^2/s
ϕ	Volume fraction occupied by particles	
ρ	Density, ...	kg/m^3
ρ_d	Density of particulate, $(N_p)/m^3$	
ρ_p	Density of soil material, ...	kg/m^3
σ	Rotor solidity, $\frac{N_b}{\pi R/c}$	
τ_w	Shear stress at wall surface, ...	$kg/(ms)$

Super and sub scripts

∞	Freestream value
air	Air
p	Particle
tip	Blade tip value

Acronyms

CFD	Computational Fluid Dynamics
DVE	Degraded Visual Environment
IGE	In Ground Effect
$MTOW$	Maximum Takeoff Weight
$MUSCL$	Monotone Upstream Centred Schemes for Conservation Laws
OGE	Out of Ground Effect
PIV	Particle Image Velocimetry

the DVE severity due to the cloud. Brownout experimental works are not common, due to the high cost and risks involved. Tanner and Wong [9], used photogrammetry, and mapped the brownout cloud generated by a $EH - 60L$ helicopter at different flight configurations, while Rodgers [14], used samplers to measure the dust concentration of a brownout cloud around a full-scale H-21 aircraft. There are also examples of small scale experiments [15,16], where the dispersed phase has been simulated using soda glass spheres or talcum powder.

1.1. Contribution and novelty

In the present work, computational fluid dynamics (CFD) is employed to analyse rotors operating IGE at different advance ratios. The Eulerian approach has been used for brownout clouds generated by rotors studied previously. Comparisons in terms of different advance ratios and different rotor thrust coefficients were performed. The effect of the fuselage has also been studied. Furthermore, the Lagrangian employed particle tracking model is presented, and obtained results are compared with the Eulerian approach and experiments [9]. This direct comparison is new in the brownout literature. Even if the models have been discussed several times, they have never been compared in the same CFD framework, so that Eulerian and Lagrangian use identical flow field. All

Table 1
Published works employing Eulerian model.

Authors (Year)	Carrier Phase model	Validation
Wenrnen et al. [17] (2006)	Vorticity Confinement	None
Haehnel et al. [18] (2008)	Vorticity Confinement	Rodgers [14]
Phillips and Brown [6] (2009)	VTM	Nathan and Green [15]
Ghosh et al. [5] (2010)	RANS	Nathan and Green [15]
Polzin et al. [19] (2011)	RANS	None
Garrick et al. [4] (2013)	RANS	Nathan and Green [15]

CFD simulations have been performed using the HMB3 (Helicopter Multi-Block) CFD solver of the University of Glasgow.

1.2. Eulerian methods for brownout

Brownout and whiteout are due to the presence of particles in the flowfield. The former involves sand and the latter snow. However, other kinds of particles can be involved such as rain, ice and even small rocks. Several works used CFD and numerical models to predict brownout. In general, the main approach is to use CFD to predict the flowfield around an operating rotor, and solve an additional set of equations for the particle motion. Some of Eulerian works for brownout are listed in Table 1

In the majority of works, the one-way coupling assumption has been adopted. It describes the dispersed phase as rare in the

fluid, and is thus possible to neglect the effect of the particles on the flowfield properties. In the past, various approaches have been used to predict the flowfield around the rotorcraft, including Vortex Tracking Model (VTM) [20] or RANS (and URANS) models with different turbulence models [5,4,21]. In the Lagrangian approach, the particles (or parcels of particles) are tracked through the flowfield and the local cloud properties are defined by their properties as they pass through a point in the flowfield. For this approach, the motion of the particles is calculated using Newton's second law. This method has the advantage of accuracy in terms of particle velocities and positions, which is fundamental for modelling interactions with the ground. However, the computational cost may become prohibitive when the amount of particles is large, like in the case of a dense brownout cloud. Previous works using the Lagrangian frame of reference are [7,22,23,1]. For Eulerian methods, the properties of the particles are assumed continuous within the field. Thus, transport equations are written and discretised, and their solution gives the properties of the cloud. Works have already been published [5,4,19] for Eulerian particle tracking. All these used the same flowfield and dust models to predict brownout. The flowfield has been solved using incompressible RANS, with a momentum source term used to introduce the rotor effect in the flowfield. In Ghosh et al. [5] validation with experimental results (by Rabbott [24]) was performed for the rotor blade loading, while Garrick et al. [4] compare UH60 rotor performance (torque coefficient) at different advance ratios with experiments. The dust model used in these works consists of a convection-diffusion equation that include the terminal velocity effect (which allows taking into account gravity) and a source term for particles uplift. A qualitative validation of the dust model used in these works is described in the Ghosh et al. [5] who compared obtained cloud shape with experiments by Nathan and Green at University of Glasgow. [15]. Results presented by Garrick et al., [4] focused on comparing the cloud at different advance ratios, including landing manoeuvres. On the other hand, Ghosh et al. [5] presented results comparing different rotor cases (single rotor, tandem, tiltrotor and quad-rotor) at different heights above the ground. Results presented in these works show that all of these variables (height above the ground, rotor layout, taxiing speed) have an impact on the developed brownout cloud. A similar Eulerian model is presented in [17,18]. In these works, the flowfield has been computed as laminar and incompressible adding the vorticity confinement method, to obtain vortices near the boundary layer. The Eulerian method used a convection equation with the terminal velocity effect and source term based on the Bangold model. However, the diffusion effect has been considered negligible. Haehnel et al. [18] presented a quantitative validation of the dust density around a H-21 helicopter, compared with results presented by Rodgers et al. [14]. They focused on the development of the brownout cloud with time. Other works about brownout using the Eulerian frame of reference have been performed by Philips and Brown [6,25,20]. In these works, the dust model is a diffusion-convective model for dust, including source terms. Philips and Brown validated both their flowfield and dust models with experimental results, the former quantitatively using Lee et al. work [26] and Preston et al. [27] work, the latter qualitative with the Nathan and Green experiments [15]. Part of their work focused on the different development and cloud shape generated by different rotor configurations (mainly between tandem and single rotor), at different forward flight conditions. Results presented by Philips and Brown also include the effect of rotor blade twist on the dust cloud.

Table 2
Forward flight and rotor geometry data.

V_∞ [kts]	10	5	2.5
V_∞ [m/s]	5.14	2.57	1.1
Re	144'500	72'200	36'200
μ	0.0233	0.011	0.005
N blades	4	4	4
R [m]	5.5	5.5	5.5
c [m]	0.41	0.41	0.41
σ	0.095	0.095	0.095

2. Numerical models

2.1. CFD solver

The HMB3 (Helicopter Multi-Block) [28,29] is used for all CFD calculations in this work. It solves the Unsteady Reynolds Averaged Navier-Stokes equations (URANS) in integral form with ALE formulation (Arbitrary Lagrangian Eulerian) for time-dependent domains (moving boundaries). URANS equations are discretised using a cell-centred finite volume approach on a multi block structured grid. HMB3 uses the Osher [30] and Roe [31] approximate Riemann solvers to evaluate the convective fluxes, and the viscous terms are discretised using second order central differencing. Third order accuracy in space is provided by the Monotone Upstream Centred Schemes for Conservation Laws (MUSCL) [32]. To avoid non-physical spurious oscillations, HMB3 uses the alternative form of the Van Albada limiter [33] where large gradients exist in the flowfield. An implicit dual time stepping method is employed to perform the temporal integration. Overset grids (used in this work) [34] and the sliding plane [35] methods are available in HMB3 to allow for the relative motion between mesh components, representing ground and rotor blade. Various turbulence models are available in HMB3, including one-, two-, three- and four- equation turbulent models. Large-eddy Simulation (LES), Detached-Eddy Simulation (DES) and Delay-Detached-Eddy Simulation (DDES) can also be used with HMB3.

2.2. Forward flight and hover setup

The forward flight conditions and the rotor geometric data are listed in Table 2. Three advance ratios have been computed. Furthermore, for all test cases, two disk loading configurations have been tested. The wake structure of a forward flight rotor strongly depends on its taxiing speed. At lower taxiing speed, a recirculation region is formed in front of the aircraft, while in the case of higher taxiing speed the flowfield develops to a horseshoe vortex. The particle tracking analyses performed in this paper were strongly influenced by the obtained wakes. Two different wake patterns may generate different scenarios in terms of brownout clouds. Furthermore, using two different thrust coefficients for the same helicopter in forward flight, shows how the weight influences the dust cloud. The influence of the fuselage has also been studied, with simulations for low advance ratio with and without it. Previous works [36,37], show how helicopters with higher disk loading, in hover, generate the most dangerous scenarios. In this work, a similar analysis was performed for the forward flight case. Hover was approximated using low advance ratio forward flight, with an almost zero V_∞ (Table 3).

Flowfield calculations were performed with a chimera mesh system, using background and foreground grids. The mesh setup is presented in Fig. 1. The inner grid contains the fuselage geometry, and it is of cylindrical shape. It contains approximately 15 million cells. The fuselage was an approximate shape of a utility helicopter [38]. On the other hand, the background mesh was Cartesian. It was refined near the ground and near its centerline, following [38].

Table 3
Simulations performed for Eulerian particle tracking.

V_∞ [kts]	Mesh	C_T	Steady/Unsteady
0 (Hover)	low μ	0.0125	Steady
0 (Hover)	low μ	0.0175	Steady
5	low μ	0.0125	Steady
5	low μ	0.0175	Steady
10	low μ	0.0125	Steady
10	low μ	0.0175	Steady
10	low μ (without fuselage)	0.0125	Steady
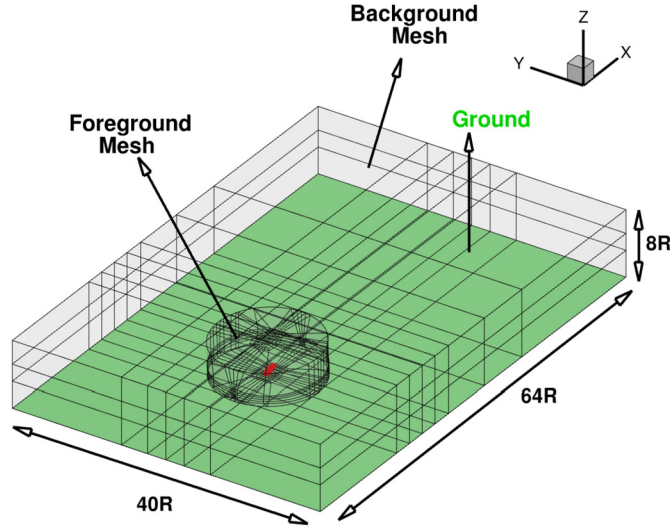
Fig. 1. Forward Flight Grid Setup.

For this taxiing speed, the wake is expected to extend in the spanwise direction, in this case, the width is 40R, while the stream wise length is about 64R as shown in Fig. 1. The background mesh contains 30 million points. The ground has been computed as a solid moving wall, moving with the freestream velocity. The rotor has been modelled with a steady, non uniform actuator disk [39]. Previous works considered a similar setup for analysis of wake encounters [40,38].

2.3. Threshold model

The Bangold model (see [41,42]) has been used in several brownout works to simulate particle uplift. Based on this model, Shao et al. [43] proposed a threshold formulation that has been adopted in this work. The threshold model is based on the wall friction velocity $u_* = \sqrt{\dfrac{\tau_w}{\rho}}$, and a threshold value that depend on particle and fluid properties as:

$$u_t^* = \sqrt{A\left(\frac{\rho_p}{\rho_{air}} g d_p + \frac{\beta}{\rho_{air} d_p}\right)}, \tag{1}$$

where A and β are coefficients: A=0.0123, β=0.0003 $\dfrac{kg}{s^2}$. The particle values, used in this work, are listed in Table 4, while for air and gravity acceleration the following values have been used: $\rho_{air} = 1.225 kg/m^3$ and $g = 9.81 m/s^2$. Particle properties are chosen to be closer to real sand grains, as described in [44]. When $u^* > u_t^*$ particles are uplifted and entrained the flowfield.

2.4. Particle motion equation

For Lagrangian particle tracking, an in-house simulation method has been used. The tool can compute particle paths for mass and

Table 4
Properties of particles used in this work.

ρ_p (kg/m^3)	d_p (μm)	C_D	B (kg/m^2)	u_t^* (m/s)
2650	9	1.048	0.03	0.58

massless particles. Both particles types are driven by the flowfield velocities and their positions in time are obtained by integrating their equations of motion. The integration method used is a fourth order Runge-Kutta. In the case of massless particles, there is no slip between a particle and the flowfield. In other words, particle and flowfield velocities are equal ($\mathbf{u} = \mathbf{u_p}$), where $\boldsymbol{u}_p$ is particle velocity and $\boldsymbol{u}$ is the velocity of the flowfield at the position of the particle. Particles have first to be localized in the computational domain to obtain the velocity of the flowfield in their particle positions. Then, to obtain the particle position it is necessary to integrate the particle motion equation. The position of the particle x_p is computed by:

$$\frac{\partial \mathbf{x}_p}{\partial t} = \mathbf{u}(t_n, \mathbf{x}_p^n). \tag{2}$$

For particles with mass, the particle and flowfield velocities are not the same, and the particle acceleration has to be computed, using:

$$\mathbf{a}_p = \frac{0.5\rho_{air}(\mathbf{u} - \mathbf{u}_p)||(\mathbf{u} - \mathbf{u}_p)||}{B} - \mathbf{g} \tag{3}$$

Here, $\boldsymbol{a}_p$ is the acceleration of the particle, $\boldsymbol{u}_p$ is its velocity, $\boldsymbol{u}$ is the velocity of the flowfield in the position of the particle and B the particle ballistic coefficient, $B = \dfrac{m_p}{S_p C_D}$. Also, m_p is the particle mass, $S_p = \pi d_p^2/4$ is the particle frontal area (particles are assumed spherical), C_D is the particle drag coefficient, and $\mathbf{g}$ is the acceleration of gravity. The particle properties used in this work are listed in Table 4, and correspond to the size and density of particles used in earlier brownout experimental and computational works [44,22,45]. The particle motion equation has been non-dimensionalized using the flowfield reference values for length, velocity and density. The reference value l_{ref} is the rotor blade chord, c, V_{ref} is V_∞, i.e. the rotor forward speed and, $\rho_{ref} = 1.225 kg/m^3$. To integrate the particle acceleration, the fourth order Runge-Kutta method has been used. To obtain the velocity and position of particles at any time step, it is necessary to integrate two vector equations, one to obtain the particle's velocities, one for its position.

2.4.1. Search algorithms

During the particle tracking process, it is necessary to know the flowfield properties in the space occupied by the particle. In other words, the particles have to be localized inside the computational domain. Two search methods are included in the Lagrangian particle tracking code. The first is used when the flowfield is seeded with particles for the first time. The distances between their starting positions and the centers of the grid cells are computed. The seeding particle is then assigned to the nearest cell in the domain. This "brute force" search method is expensive in terms of computational cost, and it is done only during the first time step to have the starting particle positions. The second search method is used after the first search, to update the particle position inside the domain, using the initial positions. To avoid the high computational cost, the search area is delimited around the neighbour cells of the particle's position at time t_n. The search area is within by the maximum distance travelled by the particle during the Δt between time instances t_n and t_{n+1}. The area is delimited by the maximum range, r_{max}, computed as: $r_{max} = ||\mathbf{u}_p||\Delta t$. A cell, i, is considered in the search area if $r_i < r_{max}$, where r_i is the distance between the

cell centre x_i, and the position of the particle at t_n, $r_i = ||\mathbf{x}_p^n - \mathbf{x}_i||$. The particle is then searched in the delimited area, comparing the distance between the cell centre and the particle position at t_{n+1}. Finally, the particle is assigned to the nearest cell. Furthermore, once a particle is found, an interpolation is performed to obtain the flowfield properties at locations of the particle. The influence of all the cells around the particles are weighted with respect to their distance from the position of the particle. In all simulations, the grids were multi-block structured with hexahedal cells, so the cells around the one contain the particle, are 27 in total, except for cells near domain boundaries.

The employed equations are:

$$u_{flow}(x_p^{n+1}) = \sum_{i=0}^{27} u_{flow}(x_i)q_i, \tag{4a}$$

$$d_i = ||\mathbf{x}_i - \mathbf{x}_p^{n+1}||, \tag{4b}$$

$$q_i = \frac{\frac{1}{d_i}}{\sum_{i=0}^{27} \frac{1}{d_i}}, \tag{4c}$$

where $u_{flow}(x_p^{n+1})$ is the flowfield velocity in the position occupied by the particle and $u_{flow}(x_i)$ the flow velocity as the centre of the i-th cell. $\mathbf{x}_i$ is the position of the i-cell centre, while $\mathbf{x}_p^{n+1}$ is the particle position at time step n+1. A particle is near the domain boundaries, its neighbours cells are fewer. In that case the interpolation is using the "halo cells" of the mesh. Two layers of halo cells are added at the boundary of the domain, and these contain the information of the first two layers of cells inside the domain of the neighbour block. This way, it is always possible to interpolate values from 27 cells. When the code runs in parallel every particle is associated with a single processor, which searches only for the particle assigned to it.

2.5. Eulerian method

The particle dust transport model used here is:

$$\int_V \frac{\partial \rho_d}{\partial t}dV + \int_V (\mathbf{u}+\mathbf{w_t}) \cdot \nabla \rho_d dV = \int_S \mathbf{S_d} \cdot \mathbf{n}dS + \int_V \nu_p \nabla^2 \rho_d dV \tag{5}$$

and start using a number density: $\rho_d = \frac{N_p}{V}$ $[N_p/m^3]$ where w_t is the fall out velocity, which takes into account the effect of gravity with, ν_p the particle diffusion coefficient, and S_d the source term, computed starting from the uplift Bangold method. To model the fall out velocity, the formula presented by Cheng has been used [46]. The same formula has been used in other Eulerian brownout works, [6]. The fall out velocity is computed starting from the dimensionless particle diameter: $d_\star = d_p \left(\frac{gb}{\nu_\infty^2}\right)^{1/3}$, with $b = \frac{\rho_p - \rho_\infty}{\rho_\infty}$. The fall out velocity is a vector, and considering the gravity direction as z, it can be written as $\mathbf{w_t} = [0\ 0\ \hat{w}_t]^T$, with

$$\hat{w}_t = \frac{\nu_\infty}{d_p}\left(\sqrt{25 + 1.2d_\star^2} - 5\right)^{1.5} \tag{6}$$

The source term can be modelled using the mass fluxes defined by Marticorena [47], in the horizontal (Q) and vertical (F) direction. In this case, the x and y axis define the ground plane, while z is normal to it. We define $\mathbf{F_m} = [Q\ Q\ F]^T$. It is necessary start with the horizontal, computed starting from the threshold friction velocity.

$$Q = Ecu_*^3 \frac{\rho}{g}\left(1 - \frac{u_t^*}{u_*}\right)\left(1 + \frac{u_t^{*2}}{u_*^2}\right) \tag{7}$$

Where u_{*t} is the threshold friction velocity (Bangold model), while $u_{*t} = \sqrt{\frac{\tau_w}{\rho}}$ is the friction velocity. Furthermore, $c = 0.261$ is a coefficient of the model, ρ is the flowfield density, and E is the ratio of erodible to total surface area, taken as 1 for simplicity. From the horizontal flux, it is possible to compute the vertical flux [47] as:

$$F = Q\,e^{13.4f-6.0} \tag{8}$$

In this work the parameter was set to f=0.1, following [47]. The vertical flux F is defined in [47] as the mass of fine particles passing thought a horizontal unit area per unit time. The equation derived by Manticorena [47], is defined as a mass flux, with units of $[\frac{kg}{ms}]$. To use it for the source term, it must be modified to obtain a flux as number of particles per unit volume. The flux mass has been modified as: $\mathbf{S_d} = [Q\ Q\ F]^T \frac{d_p}{m_p A_p}$. Where m_p is the particle mass, d_p is the particle diameter and A_p the particle frontal area, which can be considered the smallest area through a particle can enter the flowfield from the ground. Then,

$$Q\frac{d_p}{m_p A_{ref}} = \frac{Ecd_p}{m_p A_{ref}}u_*^3\frac{\rho}{g}\left(1 - \frac{u_t^*}{u_*}\right)\left(1 + \frac{u_t^{*2}}{u_*^2}\right) = \frac{pu_*^3}{m_p A_{ref}}\frac{\rho d_p}{g} \tag{9}$$

where $p = Ec\left(1 - \frac{u_t^*}{u_*}\right)\left(1 + \frac{u_t^{*2}}{u_*^2}\right)$, and contains only dimensionless values. It is important to notice that if $u_{*t} > u_*$, the threshold model is not satisfied, in other words, particles cannot be uplifted, and this may lead to a zero flux, leading to $S_d = 0$, in case of $u_{*t} > u_*$. We now define ϕ, the volume fraction occupied by the particles as $\phi = \rho_d V_p$. To obtain this, we can multiply both sides of equation with V_p, volume of the particle. It also necessary to apply the divergence theorem to the source term in equation (5), to obtain:

$$\int_V \frac{\partial \phi}{\partial t}dV + \int_V (\mathbf{u} + \mathbf{w_t}) \cdot \nabla\phi dV = V_p\int_V \nabla \cdot \mathbf{S_d}dV + \int_V \nu_p \nabla^2 \phi dV \tag{10}$$

Considering an arbitrary volume, we can obtain:

$$\frac{\partial \phi}{\partial t} + (\mathbf{u} + \mathbf{w_t}) \cdot \nabla\phi = V_p\nabla \cdot \mathbf{S_d} + \nu_p \nabla^2 \phi \tag{11}$$

It is now necessary to non-dimenzionalize equation (11), using:

$$\tilde{t} = \frac{t}{l_{ref}/V_{ref}}$$
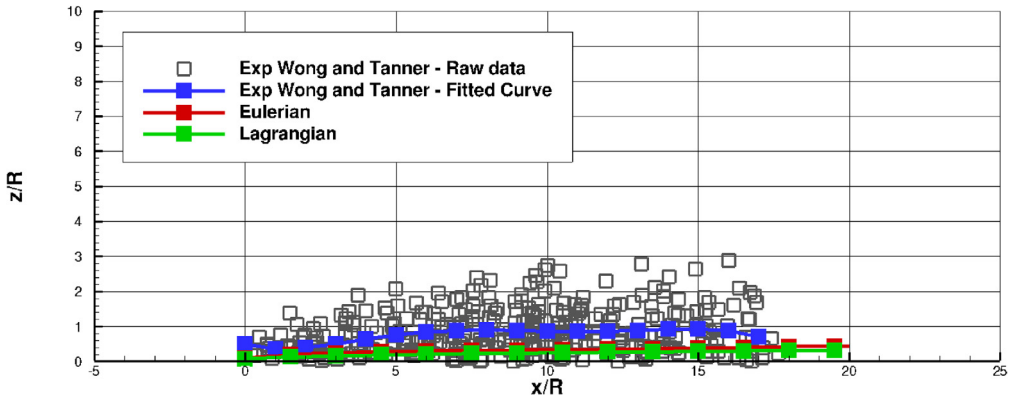$$\tilde{x} = \frac{x}{l_{ref}} \tag{12}$$

and define $\sigma = \frac{\rho}{\rho_p}$, which is the ratio between the density of the fluid and the density of particles material soil ($\rho_p = 2650kg/m^3$). We also define the ratio between the particle diameter and the reference length: $\hat{d}_p = \frac{d_p}{l_{ref}}$.

Rewriting the expression, with the dimensionless variables, we obtain:

$$\frac{\partial \phi}{\partial \tilde{t}}\frac{V_{ref}}{l_{ref}} + (\tilde{\mathbf{u}} + \widetilde{\mathbf{w_t}}) \cdot \nabla\phi\frac{V_{ref}}{l_{ref}} = \frac{V_p}{l_{ref}}\nabla \cdot \mathbf{S_d} + \nabla^2\phi\frac{1}{l_{ref}^2}\frac{\nu}{Sc} \tag{13}$$
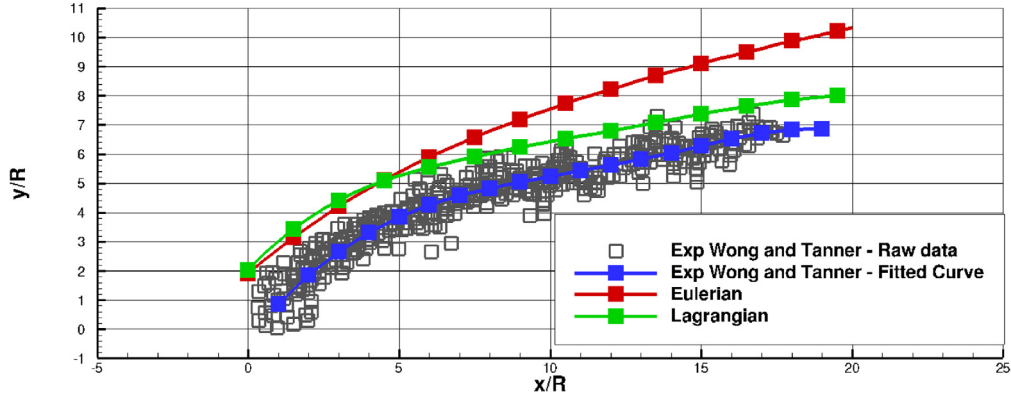
(a) Top View

(b) Side View

Fig. 2. Validation of the Eulerian and Lagrangian models. Experiments (gray dots) [9] vs present study results. The rotor was operating at $\mu = 0.058$, $C_T = 0.017$. Particle properties are listed in Table 4.

and with some algebra, it is possible to obtain:

$$\frac{\partial \phi}{\partial \tilde{t}} + (\widetilde{\mathbf{u}} + \widetilde{\mathbf{w_t}}) \cdot \nabla \phi = \frac{V_p}{V_{ref}} \nabla \cdot \mathbf{S_d} + \nabla^2 \phi \frac{1}{Sc} \frac{1}{Re} \quad (14)$$

where $\mathbf{n}$ can be defined as $\mathbf{n} = [0\ 0\ 1]^T$, in this way:

$$\nabla \cdot \mathbf{S_d}$$
$$= \left(\frac{\partial}{\partial x} \left(p \widetilde{u_*}^3 \right) + \frac{\partial}{\partial y} \left(p \widetilde{u_*}^3 \right) + \frac{\partial}{\partial z} \left(p \widetilde{u_*}^3 \right) e^{13.4f-6.0} \right) \frac{V_{ref}^3 \rho V_p d_p}{g m_p A_p} \quad (15)$$

$$\frac{\partial \phi}{\partial \tilde{t}} + (\widetilde{\mathbf{u}} + \widetilde{\mathbf{w_t}}) \cdot \nabla \phi$$
$$= \left(\frac{\partial p \widetilde{u_*}^3}{\partial x} + \frac{\partial p \widetilde{u_*}^3}{\partial y} + \frac{\partial p \widetilde{u_*}^3}{\partial z} e^{13.4-6.0} \right)$$
$$\times V_{ref}^3 \frac{V_p \rho}{g} \frac{1}{\rho_p V_p \frac{\pi \hat{d}_p l_{ref}}{4}} \frac{1}{V_{ref}} + \nabla^2 \phi \frac{1}{ScRe} \quad (16)$$

Defining $S = \left(\frac{\partial p \widetilde{u_*}^3}{\partial x} + \frac{\partial p \widetilde{u_*}^3}{\partial y} + \frac{\partial p \widetilde{u_*}^3}{\partial z} e^{13.4-6.0} \right)$, for simplicity, and using the first term on the right of equation we obtain:

$$S V_{ref}^3 \frac{\rho}{g} \frac{V_p}{\rho_s V_p \frac{\pi \hat{d}_p^2 l_{ref}^2}{4}} \frac{l_{ref}}{V_{ref}} = S V_{ref}^2 \frac{4\sigma V_p}{g \pi \hat{d}_p} \quad (17)$$

Introducing $\sigma = \frac{\rho}{\rho_s}$ and the Froude number as $Fr^2 = \frac{V_{ref}^2}{g l_{ref}}$ we have:

$$\frac{\partial \phi}{\partial \tilde{t}} + (\widetilde{\mathbf{u}} + \widetilde{\mathbf{w_t}}) \cdot \nabla \phi = S \frac{4Fr^2 \sigma}{\pi \hat{d}_p} + \nabla^2 \phi \frac{1}{ScRe} \quad (18)$$

The Sc number can be modelled using the Einstein-Stokes equation for brownian motion. [48]. Then,

$$\nu_p = \frac{kT}{3\pi \mu d_p}, \quad (19)$$

where k is the Boltzmann constant, T is the temperature, μ is the fluid viscosity, and as usual d_p particle diameter.

3. Results

3.1. Validation test case - EH-60L Wong and Tanner experiments

Eulerian model and Lagrangian particle tracking have been validated using experimental results obtained by [9]. Experiments have been performed using photogrammetry to obtain qualitative results of the brownout cloud development of a EH-60L taxiing. The aircraft was operating at around 15 m (around 1.8R) altitude and 12 m/s (approx 25 kts). A flowfield simulation has been performed for the same mesh, described previously, with a higher advance ratio ($\mu = 0.058$) and for a $C_T = 0.017$. The ground has been seeded considering a density of particles on the ground around 8 particles /m^2, with particles covering all areas where the friction
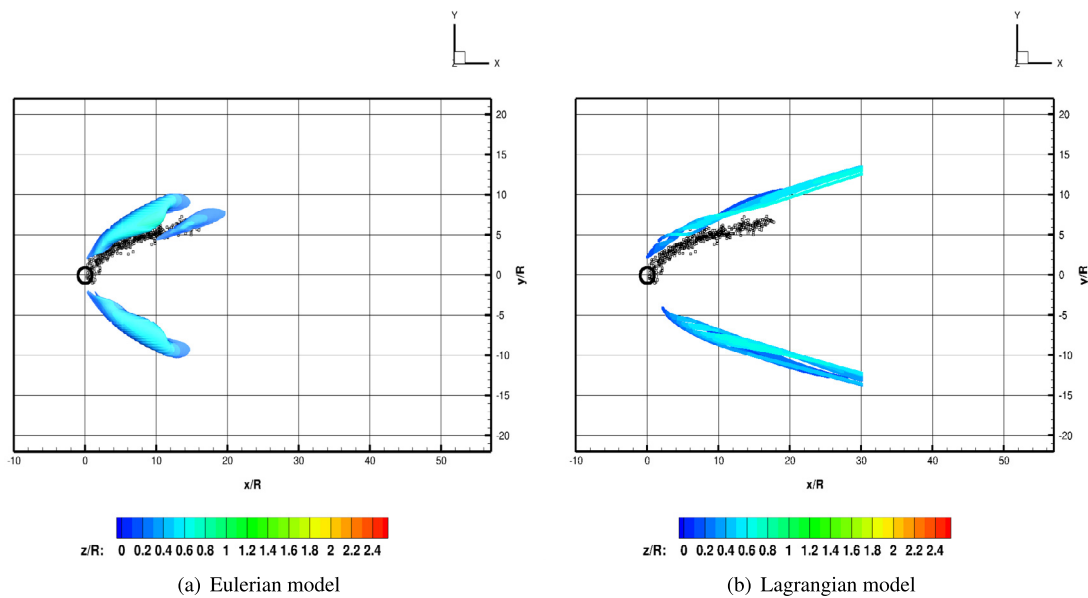
Fig. 3. Lagrangian particle tracking and Eulerian Particle Tracking Validation. Experiments (black dots) [9] vs present study results (dots/isosurfaces with contours). The rotor was operating at $\mu = 0.058$, $C_T = 0.017$. Particles properties listed in Table 4.

threshold model is satisfied. The experiment results show the development of the cloud at different time steps. To compare these unsteady results with steady state simulations, experimental results have been collected in a single cloud shape. The aircraft position was then moved to the origin of the domain, while the relative position between the aircraft position and the cloud points was preserved. In these simulations, particles have the properties listed in Table 4. The number of particles per square unit has been chosen as a trade-off between the finite computing resources available, and the need to have enough particles in the flowfield to represent the brownout cloud. Even if the number may appear small, the final cloud, counts millions of particles. Fig. 2, quantifies the differences between the experimental results and the numerical simulations. Considering the difficulties of comparing different clouds in terms of shape and size, the clouds have been approximated with a polynomial curve obtained using the least squares method.

Fig. 2 (A) is a top view. As can be seen in Fig. 2 (A), closer to the rotor (for $X/R < 5$), the two numerical methods present similar results, with a distance of $0.3R$ at $X/R = 1.5$. While the distance between the experiments and the numerical methods is about 1R for $X/R < 5$. Furthermore, when the distance from the rotor increases, the two numerical methods slightly differ. For $X/R > 5$, the Lagrangian method is more accurate, preserving an error of 1R with experiments. This error is almost constant for all the range of X/R considered, and the shape of experimental results, is close to the numerical. On the other hand, Eulerian results worsen further from the rotor, showing up to 3R of difference with experiments at around $X/R = 20$. Fig. 2 (B) shows the side view. Here, the scatter in the experimental results is more evident, and the comparison with CFD is more difficult. However, it is noticeable that the distance between numerical and experimental data is within the scatter of experiments. Like in the top view considered previously, the two numerical methods show similar results, with a difference between the CFD and experiment of around 0.1R, while the distance between the experiments is around 0.5R. From the top view, it is possible to say that the Lagrangian is more accurate than the Eulerian method for $X/R > 5$. However, this method is limited by the amount of particles it can handle.

Full cloud results are presented in Fig. 3 and Fig. 4.

The results reveal that the Lagrangian particle tracking provides a good approximation to the brownout cloud in Fig. 3 (B). Computational and experimental results follow the wake shape, forming a parabolic dust front. A small difference can still be noticed between experimental and computational results, however, this difference can be due to the comparison between steady-state simulations and unsteady experimental results. The computational results, however, underestimate the maximum height of the cloud, showing a maximum cloud altitude around 1R, while the maximum experimental cloud reaches almost 1.5R (Fig. 4 (B)). These differences may be due to the low number of particles used in the Lagrangian code. Furthermore, in a real scenario, particles have different shapes and dimensions, instead of the uniform properties used here. In general, the Eulerian model follows the Lagrangian particle tracking results, as shown in Figs. 3 (A) and 4 (A) with similar agreement with experiments.

3.2. Particles uplift

Results in terms of uplift particle areas are now presented. To obtain these results, the Bangold model has been applied on the ground, computing the friction velocity and comparing it with the threshold proposed by Shao et al. [43]. Figs. 5, 6 and 7 show particle uplift results for two disk loading condition, and for all advance ratios simulated. In general, higher thrust coefficients lead to wider uplift areas. The uplift area increases by almost 1R at higher C_T, in all cases considered. In hover, shown in Figs. 5, the uplift area is 3420 m^2 (roughly 25A_{rotor}) for $C_T = 0.0125$, while for $C_T = 0.0175$ it grows to 4928 m^2 (approx 36A_{rotor}). Some differences are seen between the forward and aft one even if it is the hover case. This is mainly due to the presence of the fuselage. For both forward flight cases, the uplift area decreases. For $V_\infty = 2.5m/s$ shown in Fig. 6 the uplift area is about 980 m^2 (approx 10A_{rotor}) for the $C_T = 0.0125$ and 1536 m^2 (roughly 16 A_{rotor}) for $C_T = 0.0175$. The uplift area drops more by increasing the taxiing speed. In this case (Fig. 7, $V_\infty = 5.14m/s$), the uplift area is 800 m^2 (roughly 8.4 A_{rotor}) for $C_T = 0.0125$, and 1240 m^2 (approx 13 A_{rotor}) for $C_T = 0.0175$. Furthermore, it is possible to notice, how the uplift area shape changes increasing the taxing speed. For the hover case, the uplift area is almost circular, however, it became stretched downstream, with increasing taxiing speed. For higher advance ra-
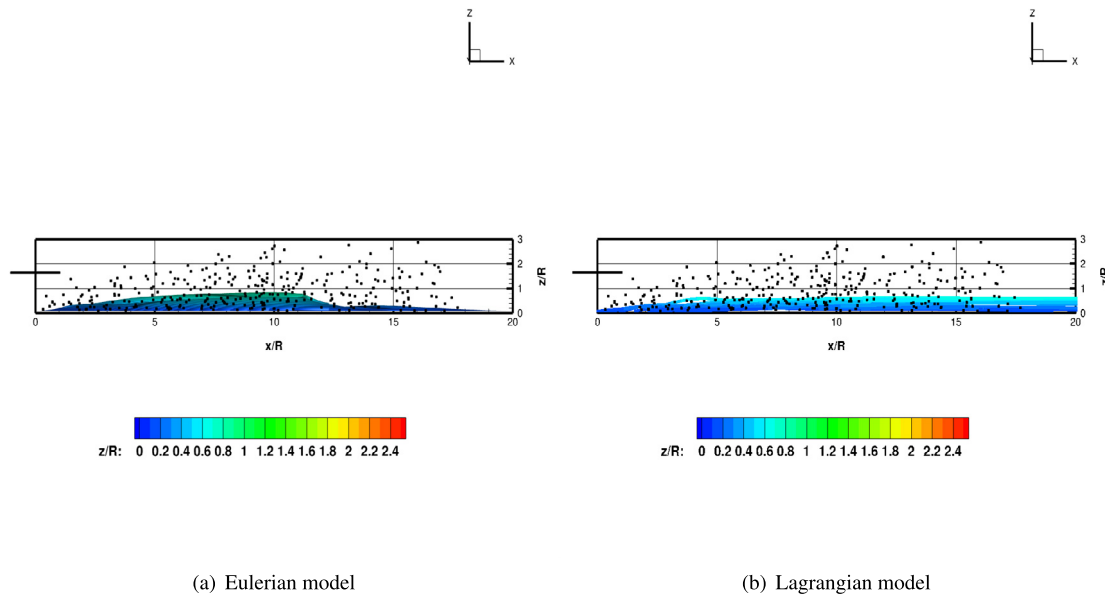
(a) Eulerian model   (b) Lagrangian model

Fig. 4. Lagrangian particle tracking and Eulerian model validation. Experiments (black dots) [9] vs present study results (dots/isosurfaces with contours). The rotor was operating at $\mu = 0.058$, $C_T = 0.017$. Particles properties listed in Table 4.
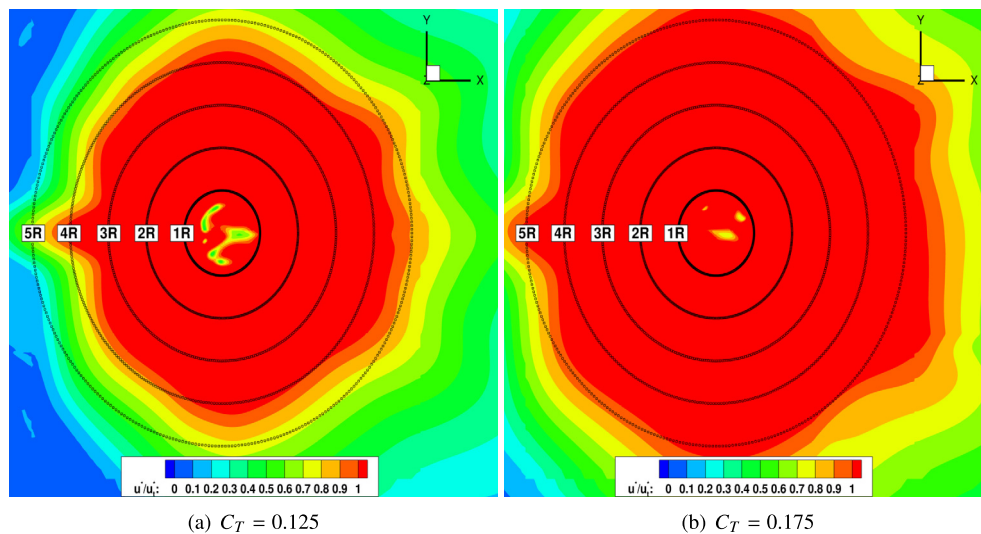

(a) $C_T = 0.125$ (b) $C_T = 0.175$

Fig. 5. Particle uplift criterion results. The rotor was operating in hover, h/R=1.66. Particles properties listed in Table 4.

tios, the uplift area extends mainly behind the rotor, while for the hover case it is almost equally distributed around the rotor describing a circle area. This is due to the change of the wake topology influenced by the different advance ratios of the simulations. The wake topology changes due to different taxiing speeds have been deeply described in previous works including [38], [49].

3.3. Lagrangian and Eulerian results comparisons

Eulerian results are now presented using isosurfaces of volume fraction occupied by dust particles (isosurfaces at $\phi = 10^{-3}$) and compared with massless Lagrangian particle tracking. These simulations are performed as steady, imposing at the first time step a 3cm sand thickness layer on the ground. On the other hand, Lagrangian particle tracking has been set up using the information extracted from the uplift analysis. To avoid further increases of execution time, the ground has been seeded with the particles only where they are more likely to be uplifted by the flowfield. The ground has been seeded considering the same density of particles

on the ground of 8 particles $/m^2$, with particles covering all areas where the friction threshold model is satisfied. Furthermore, different layers of particles have been placed at different heights on the ground, from zero up to 3cm thickness with a Gaussian distribution. As a final result, the low speed forward flight with $C_T = 0.0125$, has been seeded with 6110 particles, resulting in a final cloud of 91 million points, while the case with $C_T = 0.0175$ the particles on the ground were 10,000, resulting in a final cloud of 150 million particles. For this comparison, the particles are considered massless, and gravity has not been taken into account.

Brownout clouds computed with the Eulerian approach are now presented. In Figs. 8 (A) and (B) the clouds generated for the lowest advance ratio condition are shown. In these results, the forward speed is limited, and the case can be considered almost in hover. At this advance ratio, the effect of forward speed is minimal and the cloud surrounds the rotor in almost every direction, leaving a small clearance only behind it. For both thrust coefficients, the cloud reaches 20R distance in the lateral direction and around 20R behind the rotor. However, particles also spread in front of the air-
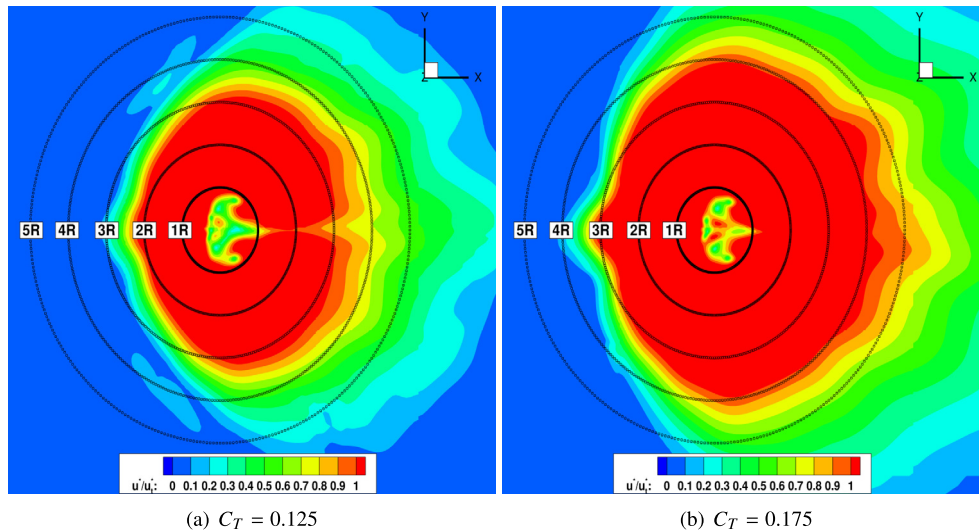
(a) $C_T = 0.125$ (b) $C_T = 0.175$

Fig. 6. Particle uplift criterion results. The rotor was operating in forward flight $\mu = 0.011$, h/R=1.66. Particles properties listed in 4.

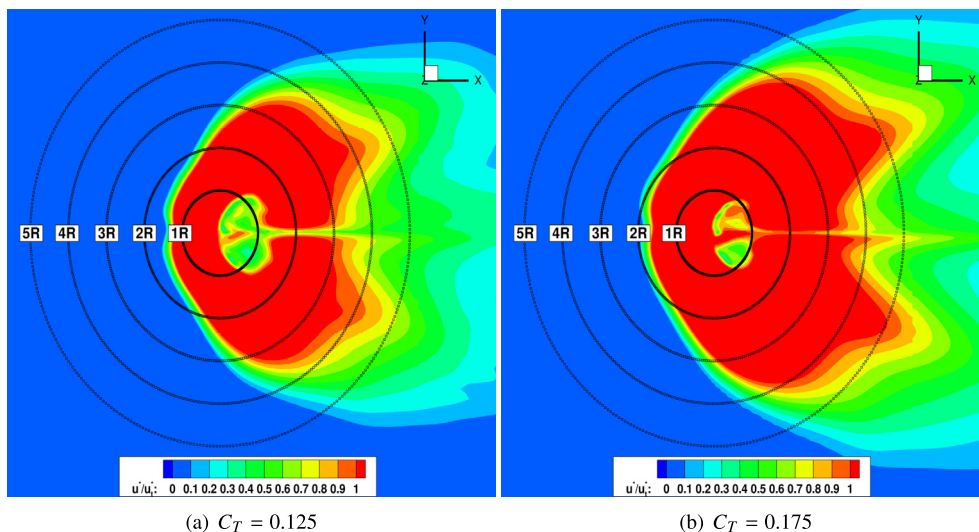(a) $C_T = 0.125$ (b) $C_T = 0.175$

Fig. 7. Particle uplift criterion results. The rotor was operating in forward flight $\mu = 0.022$, h/R=1.66. Particles properties listed in 4.

craft, generating a dense recirculation region that extends to 15R in hight. Furthermore, the particles can reach 6R height above the ground. As said, in this case, the cloud completely surrounds the aircraft, generating a severe DVE condition. The two thrust configurations show very similar results. However, when the thrust coefficient is higher, the cloud spreads more, reaching higher and further positions with respect to the other case. In general, the Lagrangian particle tracking agrees with the Eulerian results, the main cloud features can also be seen in Figs. 8 (C) and (D). However, some differences can still be noticed. The Lagrangian results show more asymmetry in the flowfield. In the Eulerian case the two sides of the cloud look similar in terms of dimensions, while the cloud side at $Y/R < 0$ expands more in the X/R direction with respect to the other side ($Y/R > 0$) for the Lagrangian methods. This may be due to the differences on ground seeding between the two models, and the limited number of particles in the Lagrangian case. Small asymmetries entities were expected in the flowfield due to the presence of the fuselage and the usage of a non-uniform actuator disk in these simulations. A comparison between the two models can also be used at higher advance ratio cases, in Figs. 9 (C) and (D). At this taxiing speed, the cloud spreads in front of the rotor and behind it, following the rotor wake. Behind the rotor, the

cloud spreads in two separate branches, that can reach a distance of 20R in the lateral direction, and 2.5R in height. This part of the brownout cloud may affect other aircraft operating nearby, spoiling their visual, or the driven dust may be ingested by their engines. Furthermore, particles may damage structures and give problems to ground personnel. As seen in previous works, higher disk loading configurations are able to generate bigger clouds [50,37]. For this advance ratio value, the two models agree better than for the previous case. The branches of the cloud are quite symmetric in all cases presented, and the cloud shape and dimensions agree among the two computational models. When the taxiing speed is further increased, the cloud is strongly influenced by the wake topology, like in the previous cases. At $\mu = 0.022$ (Figs. 10 (A) and (B)) the cloud is formed by a dense region in front of the rotor and by two branches behind the aircraft, however, some differences can still be noticed. First of all, the region in front of the rotor is smaller for the higher advance ratio, decreasing the severity of the DVE condition, with respect to the lower advance ratio case. In this case, the recirculation region stops at 4R in front of the rotor. As before, an higher thrust coefficient leads to larger and taller brownout clouds. Figs. 10 (A) and (B) can be compared with Figs. 10 (C) and (D) for a direct contrast of results obtained with the two dif-
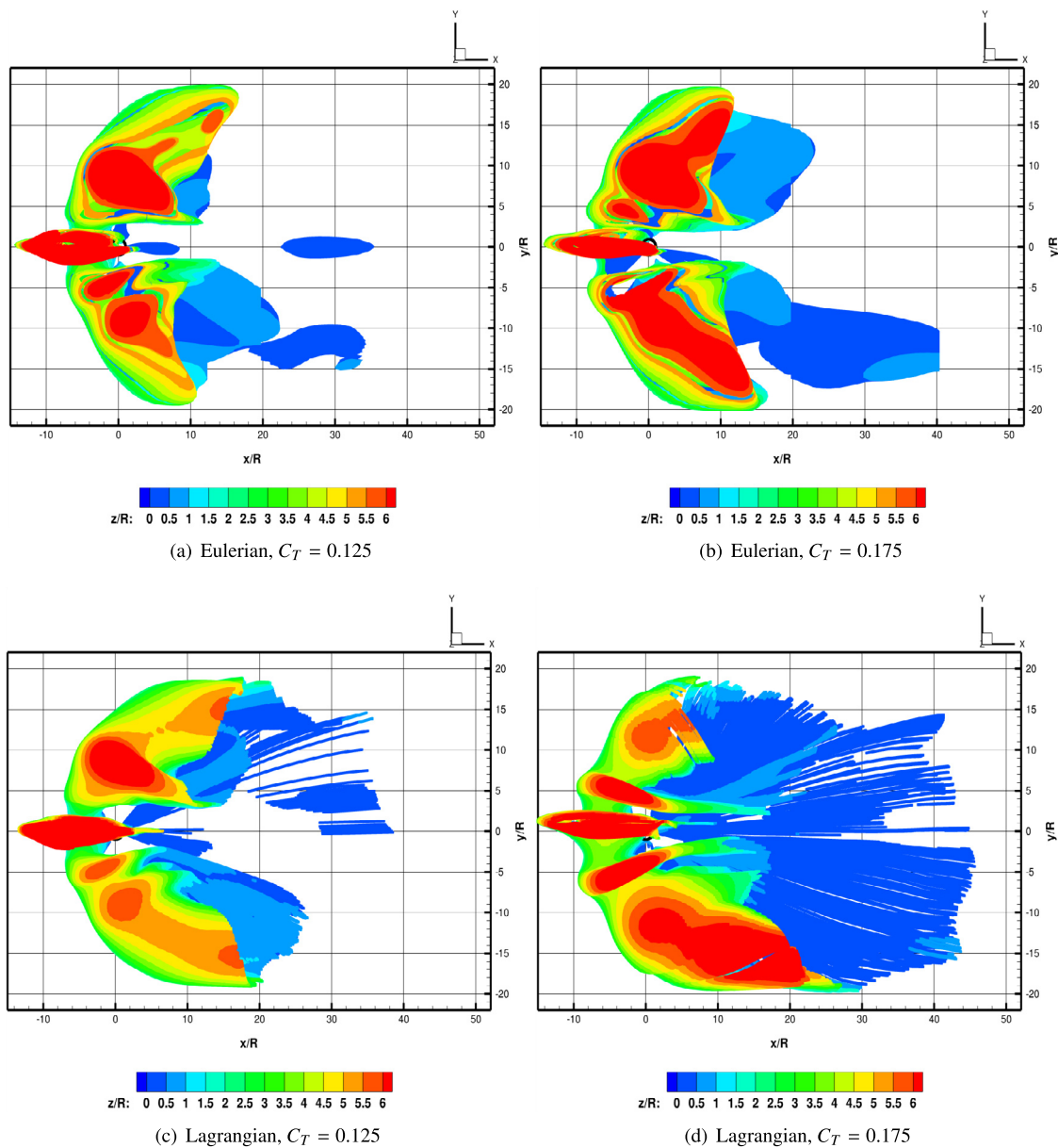
(a) Eulerian, $C_T = 0.125$

(b) Eulerian, $C_T = 0.175$

(c) Lagrangian, $C_T = 0.125$

(d) Lagrangian, $C_T = 0.175$

Fig. 8. Lagrangian particle tracking and cloud isosurfaces, with the rotor was operating in hover, h/R=1.66. Massless particles.

ferent approaches. Results are comparable mainly everywhere in the domain. Particles can reach similar results for the cloud shape, maximum height and distance reached. The final cloud is 15R wide and with a maximum height of around 3R. Furthermore, both approaches show larger clouds in the case of higher rotor thrust coefficient configurations. Comparing 10 (B) and 10 (C), it is possible to notice some differences in proximity to the rotor. In the Lagrangian case, some particles reach high positions during recirculation. This number of particles is low and they are not visible in the Eulerian results which show an isosurface of $\phi = 10^{-3}$. Fig. 11 compares the Eulerian and Lagrangian results for the no fuselage configuration. In both cases, it is possible to notice that asymmetric of the previous clouds was due to the fuselage. The clouds shown in Figs. 11 (a) and (b) look very similar. Both clouds follow the wake topology, with a limited recirculation region in front of the rotor. In this part of the cloud, the particles are not reingested by the rotor itself, however, their height is enough to spoil the visual of the pilot on the ground.

3.4. Timing and performance comparison of the methods

In this section, performance analysis is shown, comparing Eulerian and Lagrangian execution times and parallel performances. Both codes can run in serial and parallel computers. In the Lagrangian particle tracking, the total amount of particles is shared among processors. When a new particle is uplifted inside the flowfield, it is assigned to a single processor, which tracks it for the whole simulation. In general, the size of the mesh has an influence on the total execution time of Lagrangian code. Searching particles in finer meshes is computationally more expensive. However, the mesh size does not have a strong influence on parallel scaling, all processors having to read the input flowfield files. On the other hand, in the Eulerian method, the code takes advantage of the multi-block approach used in HMB3 and processors solve the transport equation for the assigned number of blocks. Blocks are shared among the processors to obtain an equal amount of work. Due to the nature of the Eulerian approach, the total amount of particles is not known a priori. A single diffusion equation is computed, independently from the number of particles that a specific
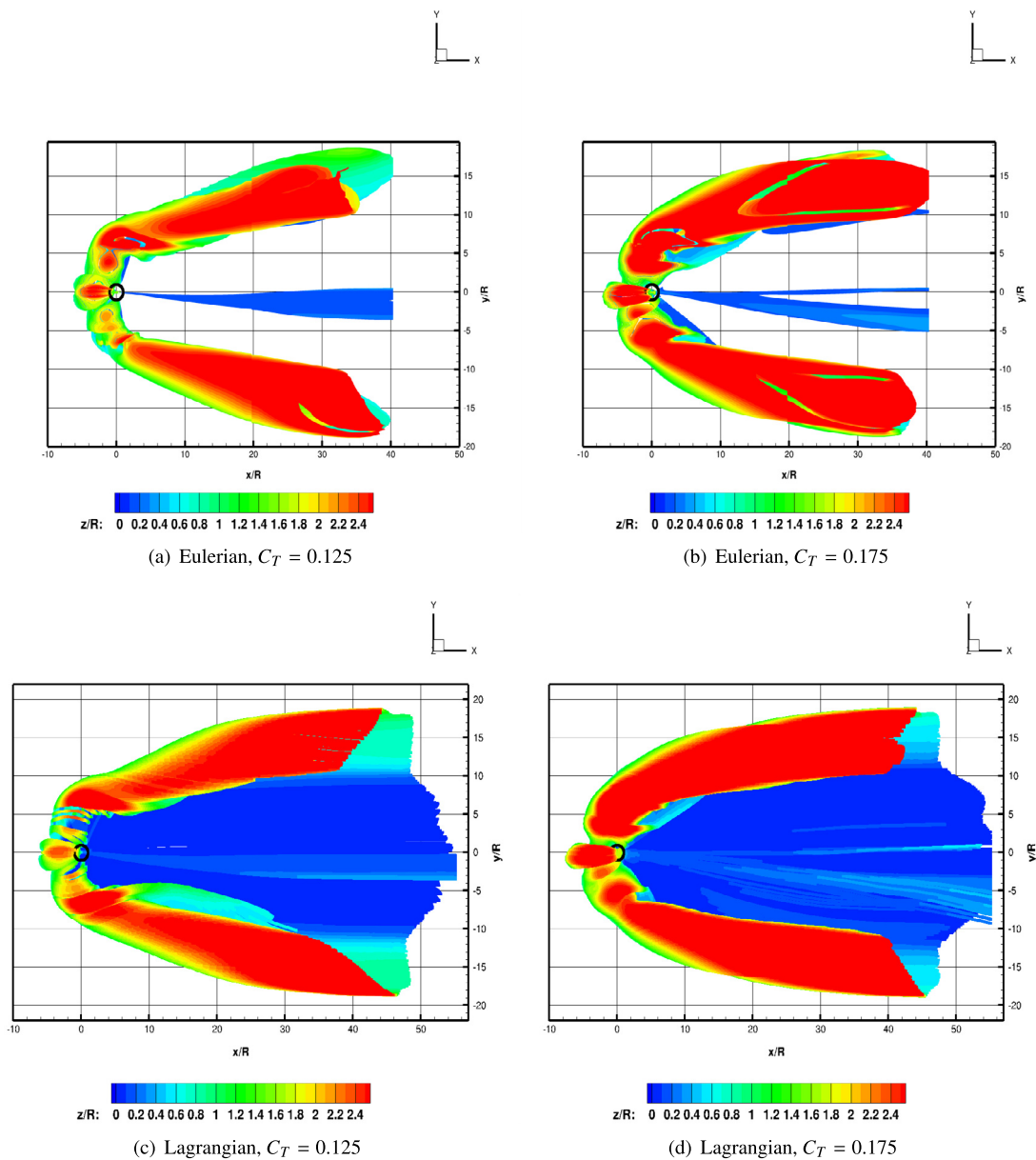
(a) Eulerian, $C_T = 0.125$

(b) Eulerian, $C_T = 0.175$

(c) Lagrangian, $C_T = 0.125$

(d) Lagrangian, $C_T = 0.175$

Fig. 9. Lagrangian particle tracking and cloud isosurfaces, with the rotor was operating in forward flight $\mu = 0.011$, h/R=1.66. Massless particles.

test case may take into account. In Fig. 12 it is possible to see how performances improve increasing number of processors. The speed up is close to the ideal-linear behaviour for a very limited number of processors in both cases, however, the Lagrangian case is closer to the ideal cases with a higher number of processors. When 8 processors used, the speed-up of the Lagrangian code is around 6.3 and 6.6 (depending on the number of particles used), while Eulerian speed up stops at 5.5. This is a function of the employed number of blocks, dividing further any more CPU can lead to better performances. It is important to say that in the Eulerian case, the amount of memory used for the simulation is limited, and shared among the processors, while in the case of the Lagrangian code, with more processors are used, more memory is needed to store the flowfield. In the Lagrangian code, to limit the number of information exchanges between processors, the flowfield is read by every processor, increasing the total amount of memory needed for the simulation.

As already said, in the Eulerian approach, the number of particles has no influence on timing performance. In general when the

amount of particles is limited, the Lagrangian approach is better than the Eulerian, it allows a faster and more accurate calculation. However as this amount grows, the total execution time becomes prohibitive. In Fig. 13 the total execution time for the Lagrangian and Eulerian codes are compared. The total execution time for Lagrangian code scales linearly with the total number of particles in the flowfield, and this execution time is computed starting from the linear behaviour computed for a smaller amount of particles [50]. On the other hand, the Eulerian execution time is independent of the number of particles. Every sub-plot of Fig. 13, emphasizes a number of particles uplifted. When the total amount of particles in the simulation is greater than the threshold, the Lagrangian execution time overcomes the Eulerian, and it became less efficient. It is also possible to notice that when the number of processors increases, the threshold grows. This is due to the fact that the Lagrangian method speed-up is faster with respect to the Eulerian, as shown in Fig. 12. The linear slope of the Lagrangian curve decreases faster than the Eulerian fixed value, as shown in Fig. 13 This is due to the larger amount of memory needed to run
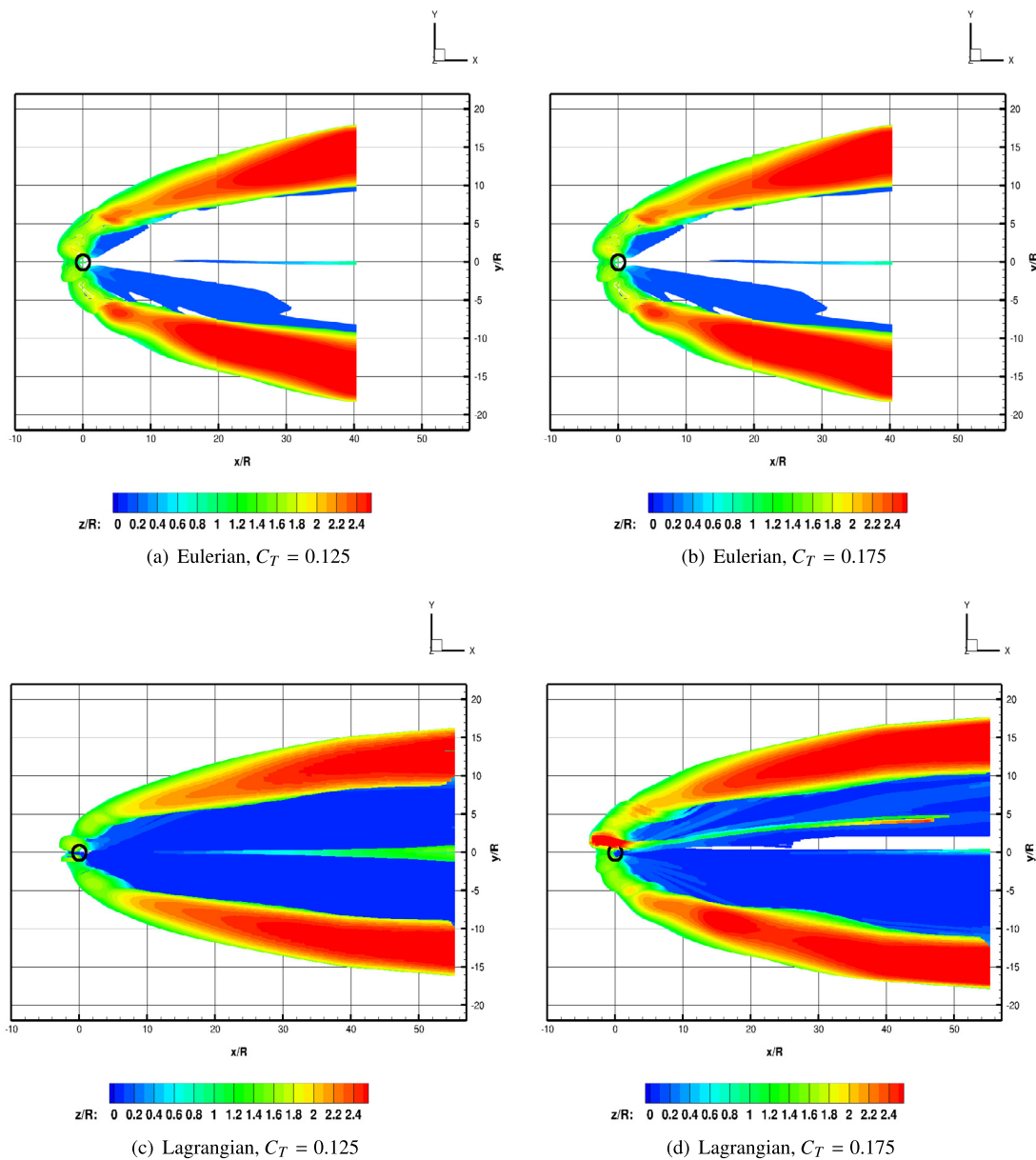
(a) Eulerian, $C_T = 0.125$

(b) Eulerian, $C_T = 0.175$

(c) Lagrangian, $C_T = 0.125$

(d) Lagrangian, $C_T = 0.175$

Fig. 10. Lagrangian particle tracking and cloud isosurfaces, with the rotor was operating in forward flight $\mu = 0.022$, h/R=1.66. Massless particles.

the Lagrangian test case. Furthermore, the Lagrangian output files contain a very large number of points, and may become difficult to post-process.

4. Conclusions and future steps

Eulerian and Lagrangian approaches have been used, in the past, for brownout simulations. In this work these two approaches have been compared using the same test cases. Results show very similar behaviour in cloud shape and size, even if some differences can be noticed. In general, brownout clouds follow the wake topology in both approaches. A dust wall is formed in front of the rotor, following the recirculation region ahead of the fuselage. However, the cloud also spreads behind the rotor, separating in two branches that cover a wide area around the flight path. Similar results have been shown for the two approaches in the test cases taken into account. Both methods agree on the cloud size, defining different clouds for different configurations of taxiing speed and disk loading. Both numerical methods show fair comparison with experimental results. The Lagrangian methods can estimate the in-

fluence of the wake on particles path, however, the limits of the code are clear when the maximum height of the clouds are compared. A limited number of particles can be computed, and this limits the final cloud shape. A more detailed analysis of Eulerian and Lagrangian results for different rotor flight configurations show good agreement between the two methods. However, the computational cost to simulate brownout clouds with Lagrangian particle tracking can be prohibitive. The execution time needed to simulate a brownout cloud is influenced by the total amount of particles in the flowfield and it may become very high. For this reason, an Eulerian approach can be considered better for brownout. Results show that the uplift of particles is influenced by the taxiing speed, and higher advance ratios lead to a smaller uplift area on the ground. Furthermore, the advance ratio also has an influence on the uplift area shape. The almost circular uplift area shown in the hover case changes increasing the taxiing speed. Furthermore, uplift and brownout simulations are shown as the disk loading configurations increase the uplift area and the cloud size, potentially leading to more dangerous scenarios for the crew and the ground
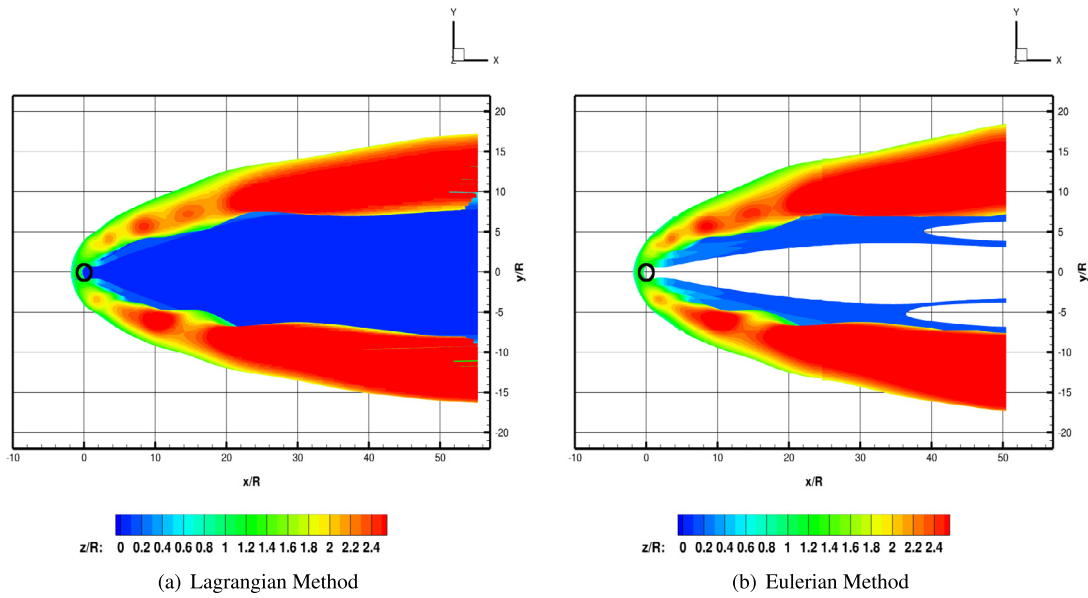
(a) Lagrangian Method   (b) Eulerian Method

Fig. 11. Lagrangian and Eulerian, without fuselage. The rotor was operating in forward flight $\mu = 0.022$, h/R=1.66. Massless particles.
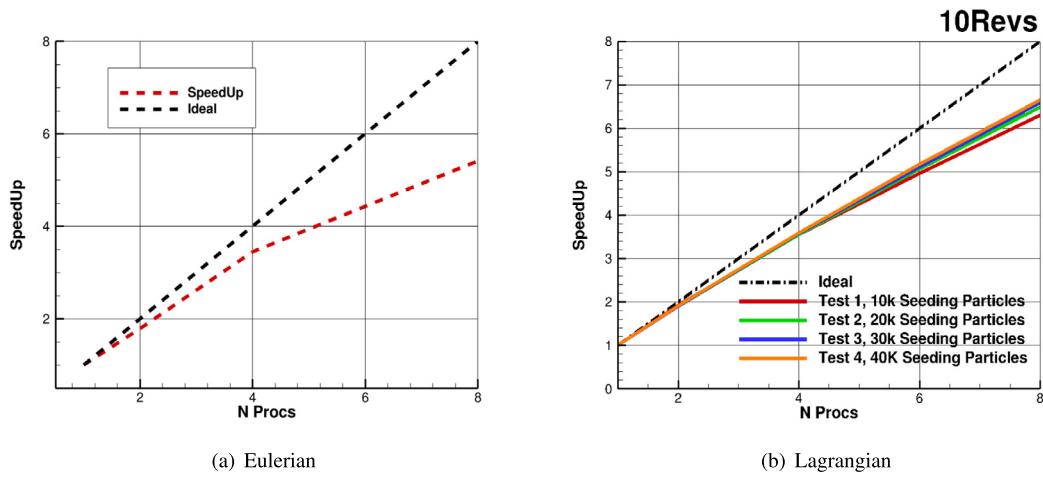

(a) Eulerian   (b) Lagrangian

Fig. 12. SpeedUp Lagrangian vs Eulerian.
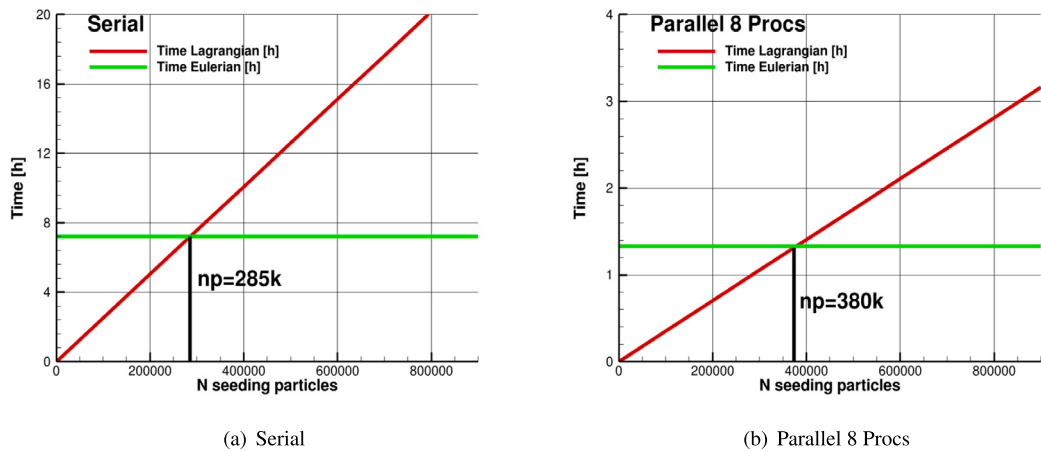

(a) Serial   (b) Parallel 8 Procs

Fig. 13. Timing Lagrangian vs Eulerian for different numbers of processors.

personnel. Similar conclusions have been reported in [21,50,37]. In all cases presented, particles keep following the wake, reaching height altitude with respect to the ground. The current results mainly cover massless particles. With mass and gravity considered, the brownout clouds may be different, but their size is expected to be smaller. For this reason, the sizes of clouds shown here, may be used for initial estimation of safety zones around hovering and taxiing helicopters.

Declaration of competing interest

The authors declare the following financial interests/personal relationships which may be considered as potential competing interests: Federico Rovere reports financial support was provided by European Union.

Data availability

Data will be made available on request.

Acknowledgements

References

[1] A. D'Andrea, F. Scorcelletti, Enhanced numerical simulations of helicopter landing maneuvers in brownout conditions, in: 66th Annual Forum of American Helicopter Society, Phoenix, Arizona, USA, 11-13 May, 2010, pp. 1084–1101.
[2] R. Taskgroup, Rotary-wing brownout mitigation: technologies and training, Tech. Rep. RTO-TR-HFM-162, NATO Sci. Technol. Org., 2010.
[3] P. Mapes, R. Kent, R. Wood, DoD Helicopter Mishaps FY85-05: Findings and Recommendations, US Air Force 13, 2008.
[4] D.P. Garrick, R.G. Rajagopalan, K. Guntupalli, Simulation of landing maneuvers of rotorcraft in brownout conditions, in: International Powered Lift Conference, Los Angeles, CA, 2013.
[5] S. Ghosh, M.W. Lohry, R.G. Rajagopalan, Rotor configurational effect on rotorcraft brownout, in: 28th AIAA Applied Aerodynamics Conference, Chicago, Illinois, USA, 2010, p. 4238.
[6] C. Phillips, R.E. Brown, Eulerian simulation of the fluid dynamics of helicopter brownout, J. Aircr. 46 (4) (2009) 1416–1429.
[7] J. Alfred, R. Celi, J.G. Leishman, Flight path optimization for brownout mitigation using a high-fidelity simulation model, J. Am. Helicopter Soc. 62 (3) (2017) 1–15.
[8] J.F. Tan, J. Er Gao, G.N. Barakos, C.L. Lin, W.G. Zhang, M.Q. Huang, Novel approach to helicopter brownout based on vortex and discrete element methods, Aerosp. Sci. Technol. 116 (2021) 106839.
[9] O.D. Wong, P.E. Tanner, Photogrammetric measurements of an eh-60l brownout cloud, J. Am. Helicopter Soc. 61 (1) (2016) 1–10.
[10] Q. Li, Y. Shi, G. Xu, L. Wu, Research on brownout characteristics of helicopter approach flight based on the unsteady momentum source model coupled with dem, Int. J. Aeronaut. Space Sci. (2022) 1–15.
[11] J.F. Tan, Y.Y. Ge, W.G. Zhang, Z. Cui, H.W. Wang, Numerical study on helicopter brownout with crosswind, Aerosp. Sci. Technol. 131 (2022) 107965.
[12] J. Hu, G. Xu, Y. Shi, S. Huang, The influence of the blade tip shape on brownout by an approach based on computational fluid dynamics, Eng. Appl. Comput. Fluid Mech. 15 (1) (2021) 692–711.
[13] J. Hu, G. Xu, Y. Shi, L. Wu, A numerical simulation investigation of the influence of rotor wake on sediment particles by computational fluid dynamics coupling discrete element method, Aerosp. Sci. Technol. 105 (2020) 106046.
[14] S.J. Rodgers, Evaluation of the dust cloud generated by helicopter rotor downwash, Tech. Rep., USAAVLABS Technical Report 67-81, March 1968, 1968.
[15] N. Nathan, R. Green, Flow visualisation of the helicopter brown-out phenomenon, Aeronaut. J. 113 (1145) (2009) 467–478.
[16] A. Sydney, A. Baharani, J. Leishman, Understanding brownout using near-wall dual-phase flow measurements, in: 67th Annual Forum Proceedings of the American Helicopter Society, Virginia Beach, VA, 2011.
[17] Y. Wenren, J. Walter, M. Fan, J. Steinhoff, Vorticity confinement and advanced rendering to compute and visualize complex flows, in: 44th AIAA Aerospace Sciences Meeting and Exhibit, Reno, 2012.
[18] R. Haehnel, M. Moulton, Y. Wenren, J. Steinhoff, A model to simulate rotorcraft-induced brownout, in: 67th Annual Forum Proceedings of the American Helicopter Society, Montreal, Canada, 2008, pp. 589–601.
[19] W. Polzin, K. Guntupalli, R.G. Rajagopalan, Discrete blade model for rotorcraft brownout, in: 29th AIAA Applied Aerodynamics Conference, 2011.
[20] C. Phillips, H.W. Kim, R.E. Brown, The flow physics of helicopter brownout, in: 66th American Helicopter Society Forum, Phoenix, AZ, USA, 2010, pp. 1273–1291.
[21] F. Rovere, R. Steijl, G.N. Barakos, CFD analysis of a micro rotor in ground effect, in, in: AIAA Scitech Forum, Orlando, Florida, USA, 2020.
[22] M. Syal, B. Govindarajan, J. Leishman, Mesoscale sediment tracking methodology to analyze brownout cloud developments, in: 66th Annual Forum of the American Helicopter Society, Phoenix, Arizona, USA, 2010, pp. 1644–1673.
[23] D. Wachspress, G. Whitehouse, J. Keller, K. Yu, P. Gilmore, M. Dorsett, K. McClure, A high fidelity brownout model for real-time flight simulations and trainers, in: 65th Annual Forum of American Helicopter Society, Grapevine, Texas, USA, 2009, pp. 1281–1304.
[24] J.P. Rabbott Jr, Static-thrust measurements of the aerodynamic loading on a helicopter rotor blade, Tech. Rep., NASA, 1956.
[25] C. Phillips, H.W. Kim, R.E. Brown, The effect of rotor design on the fluid dynamics of helicopter brownout, in: 35th European Rotorcraft Forum, 2009, Hamburg, Germany, 2009.
[26] T.E. Lee, J.G. Leishman, M. Ramasamy, Fluid dynamics of interacting blade tip vortices with a ground plane, J. Am. Helicopter Soc. 55 (2) (2010) 22005.
[27] J.R. Preston, S. Troutman, E. Keen, M. Silva, N. Whitman, M. Calvert, M. Cardamone, M. Moulton, S.W. Ferguson, Rotorwash operational footprint modeling, Tech. Rep., Missile Research Development and Engineering Center Redstone Arsenal AL (USA) Missile Guidance Directorate, 2014.
[28] R. Steijl, G. Barakos, K. Badcock, A framework for CFD analysis of helicopter rotors in hover and forward flight, Int. J. Numer. Methods Fluids 51 (8) (2006) 819–847.
[29] S. Lawson, M. Woodgate, R. Steijl, G. Barakos, High performance computing for challenging problems in computational fluid dynamics, Prog. Aerosp. Sci. 52 (2012) 19–29.
[30] S. Osher, S. Chakravarthy, Upwind schemes and boundary conditions with applications to euler equations in general geometries, J. Comput. Phys. 50 (3) (1983) 447–481.
[31] P.L. Roe, Approximate Riemann solvers, parameter vectors, and difference schemes, J. Comput. Phys. 43 (2) (1981) 357–372.
[32] B. Van Leer, Towards the ultimate conservative difference scheme. V. A second-order sequel to godunov's method, J. Comput. Phys. 32 (1) (1979) 101–136.
[33] G. Van Albada, B. Van Leer, W. Roberts, A comparative study of computational methods in cosmic gas dynamics, in: Upwind and High-Resolution Schemes, Springer, 1997, pp. 95–103.
[34] M. Jarkowski, M. Woodgate, G. Barakos, J. Rokicki, Towards consistent hybrid overset mesh methods for rotorcraft CFD, Int. J. Numer. Methods Fluids 74 (8) (2014) 543–576.
[35] R. Steijl, G. Barakos, Sliding mesh algorithm for CFD analysis of helicopter rotor–fuselage aerodynamics, Int. J. Numer. Methods Fluids 58 (5) (2008) 527–549.
[36] F. Rovere, G. Barakos, R. Steijl, Safety analysis of model-rotors, in: AIAA Aviation Forum, 2022, pp. 2021–2625, Online Event.
[37] J. Milluzzo, J.G. Leishman, Assessment of rotorcraft brownout severity in terms of rotor design parameters, J. Am. Helicopter Soc. 55 (3) (2010) 32009.
[38] M. Sugiura, Y. Tanabe, H. Sugawara, G.N. Barakos, N. Matayoshi, H. Ishii, Validation of CFD codes for the helicopter wake in ground effect, in: 43rd European Rotorcraft Forum, 2017, Milan, Italy, 2017.
[39] G.J. Leishman, Principles of Helicopter Aerodynamics with CD Extra, Cambridge University Press, 2006.
[40] S. Cavallo, G. Ducci, R. Steijl, G.N. Barakos, CFD analysis of helicopter wakes in ground effect, in: 44th European Rotorcraft Forum, Delft, the Netherlands, 2018.
[41] R. Bagnold, The Physics of Blown Sand and Desert Dunes, Methuen, London, 1941.
[42] R. Greeley, J.D. Iversen, Wind as a Geological Process: on Earth, Mars, Venus and Titan, vol. 4, CUP Archive, 1987.
[43] Y. Shao, H. Lu, A simple expression for wind erosion threshold friction velocity, J. Geophys. Res., Atmos. 105 (D17) (2000) 22437–22443.
[44] P.E. Tanner, Photogrammetric characterization of a brownout cloud, in: 67th Annual Forum of the American Helicopter Society, Virginia Beach, Virginia, USA, 2011, pp. 3039–3055.
[45] B. Kutz, T. Günther, A. Rumpf, A. Kuhn, Numerical examination of a model rotor in brownout conditions, in: 70th Annual Forum of American Helicopter Society, Montréal, Canada, 2014, pp. 2462–2484.
[46] N.-S. Cheng, Simplified settling velocity formula for sediment particle, J. Hydraul. Eng. 123 (2) (1997) 149–152.
[47] B. Marticorena, G. Bergametti, Modeling the atmospheric dust cycle: 1. design of a soil-derived dust emission scheme, J. Geophys. Res. 100 (D8) (1995) 16,415–16,430.
[48] C.T. Crowe, J.D. Schwarzkopf, M. Sommerfeld, Y. Tsuji, Multiphase Flows with Droplets and Particles, CRC Press, 2011.

[49] F. Köpp, Wake-vortex characteristics of military-type aircraft measured at airport oberpfaffenhofen using the DLR laser doppler anemometer, Aerosp. Sci. Technol. 3 (4) (1999) 191.

[50] F. Rovere, G. Barakos, R. Steijl, Safety analysis of rotors in ground effect, Aerosp. Sci. Technol. 129 (2022) 107655.